eprints@whiterose.ac.uk
https://eprints.whiterose.ac.uk/

# Ultrafast terahertz detectors based on three-dimensional meta-atoms

B. Paulillo[1,*], S. Pirotta[1,*], H. Nong[2], P. Crozat[1], S. Guilet[1], G. Xu[1,3], S. Dhillon[2], L. Li[4], A.G. Davies[4], E.H. Linfield[4], and R. Colombelli[1]

[1] Centre de Nanosciences et de Nanotechnologies, CNRS, Univ. Paris-Sud, Université Paris-Saclay, C2N – Orsay, 91405 Orsay cedex, France

[2] Laboratoire Pierre Aigrain, Ecole Normale Supérieure-PSL ResearchUniversity, CNRS, Université Pierre et Marie Curie-Sorbonne Universités, Université Paris Diderot, Sorbonne Paris Cité, 24 rue Lhomond, 75231 Paris Cedex 05, France

[3] Key Laboratory of Infrared Imaging Materials and Detectors, Shanghai Institute of Technical Physics, Chinese Academy of Sciences, Shanghai 200083, China

[4] School of Electronic and Electrical Engineering, University of Leeds, Woodhouse Lane, Leeds LS2 9JT, United Kingdom

## Abstract

Terahertz (THz) and sub-THz frequency emitter and detector technologies are receiving increasing attention, underpinned by emerging applications in ultra-fast THz physics, frequency-combs technology and pulsed laser development in this relatively unexplored region of the electromagnetic spectrum. In particular, semiconductor-based ultrafast THz receivers are required for compact, ultrafast spectroscopy and communication systems, and to date, quantum-well infrared photodetectors (QWIPs) have proved to be an excellent technology to address this, given their intrinsic picosecond-range response. However, with research focused on diffraction-limited QWIP structures ($\lambda/2$), RC constants cannot be reduced indefinitely, and detection speeds are bound to eventually meet an upper limit. The key to an ultra-fast response with no intrinsic upper limit even at tens of gigahertz (GHz) is an aggressive reduction in device size, below the diffraction limit. Here we demonstrate sub-wavelength ($\lambda/10$) THz QWIP detectors based on a 3D split-ring geometry, yielding ultra-fast operation at a wavelength of around 100 μm. Each sensing meta-atom pixel features a suspended loop antenna that feeds THz radiation in the ~20 μm³ active volume ($V_{eff} \sim 3 \times 10^{-4} (\lambda/2)^3$. Arrays of detectors as well as single-pixel detectors have been implemented with this new architecture, with the latter exhibiting ultra-low dark currents below the nA level. This extremely small resonator architecture leads to measured optical response speeds—on arrays of 300 devices—of up to ~3 GHz and an expected device operation of up to tens of GHz, based on the measured S parameters on single devices and arrays.

## Introduction

Applications of terahertz (THz) frequency radiation (loosely defined to span the 1–10 THz frequency region) range from medical imaging through to trace gas spectroscopy. Each particular application poses specific requirements on the system components, but ultra-fast operation—for either emission or detection—is usually a vital functionality (e.g., in wireless communications or in real time imaging). To date, many THz detectors (bolometers, pyroelectric crystals, Golay cells) contain thermal sensing elements that yield modest detectivities ($D^* \sim 10^9 cm\sqrt{Hz/W}$) and/or require cryogenic cooling. Furthermore, their bandwidth is normally limited to tens of kilohertz by the device thermal and/or electrical time constants ($\tau \sim$ms)[5] [1]. Recently, superconducting hot-electron bolometer (SHEB) technology has enabled sensitive and fast responses, which suits niche applications (e.g., heterodyne receivers for astronomy). The best available NbN SHEBs exhibit high responsivities ($\approx$kV/W) and fast response times (~50 ps) up to 6 THz [2]. For lower frequencies, electronic circuit detectors (e.g., Schottky diodes or field-effect transistors) are in general excellent

1

solutions in the sub-THz frequency range [3]. Renewed interest in compact, semiconductor-based ultra-fast THz detectors has recently appeared, underpinned in part by applications in ultra-fast THz physics [4,5], frequency-comb technology [6,7], and pulsed laser development [8–10]. For instance, graphene and related 2D materials are extensively investigated as sensing elements for THz radiation, owing to their ultra-fast carrier dynamics and possible integration with the silicon platform [11]. Recently fabricated devices show a 50 ps rise time, although a responsivity only of the order of nA/W was reported [12].

To date, the most reliable THz receivers combining ultra-fast response (bandwidth in the tens of GHz) and good responsivity ($\approx$A/W) exploit a mature, solid-state technology such as the quantum-well infrared detector (QWIP) [13]. In the mid-infrared (8 µm<$\lambda$<12 µm), QWIPs are at an advanced development stage and are used as single-element detectors and as imaging cameras. In the THz range (2 – 5 THz), QWIP technology is limited to low temperatures, with typical background-limited infrared temperatures ($T_{blip}$) of $\sim$ 15⁄20 K [14]. The material system employed is usually GaAs/AlGaAs, although interest has arisen recently in the GaN platform [15]. QWIP technology is promising for efficient THz photon detectors with an ultra-fast response, owing to the short lifetime of intersubband (ISB) transitions ($\tau_{ISB}\approx$ ps). Indeed, when the material carrier dynamics is intrinsically ultra-fast, the only limitation to the detector frequency response arises from the device size i.e., the electrical RC constant of the optoelectronic component plus the read-out circuit. In a very recent paper, Li et al. report a measured bandwidth of 6.2 GHz for a THz QWIP processed in a 400 µm × 400 µm mesa geometry [16]. This demonstration has been possible by exploiting the beating between Fabry – Perot modes of a 6-mm-long THz quantum cascade laser (QCL). Before that, the best measured speeds were limited to the megahertz (MHz)/sub-MHz range [17, 18]. However, to further reduce the RC time constant and develop an architecture with the potential of response bandwidths in the tens of GHz at THz frequencies, an ultra-small, micrometre-sized resonator geometry is crucial. Unlike in the NIR/MIR range [19], this is challenging because it means operating in the extreme sub-wavelength limit. (Constraints exist linked to the lack of readily available THz QC lasers with fast modulation capabilities, but this is beyond the scope of this paper.)

To date, THz QWIPs have mainly been embedded in large (compared with the wavelength) photonic structures, such as mesas (normally substrate-coupled through a polished facet) [13, 15] or metal diffraction gratings [20]. More recently, arrays of diffraction-limited ($\lambda$⁄2) patch antennas [21] and planar meta-surfaces [22] have been used to couple radiation into THz quantum well detectors. Indeed, meta-materials are appealing as in-coupler elements for ultrafast and small THz sensors. They rely on extremely sub-wavelength single units called meta-atoms, whose archetypical example is the split-ring resonator: a sub-wavelength LC circuit where the microscopic capacitor can, in principle, host a semiconductor active region. Passive devices (absorbers, polaritonic structures, 3D metamaterials) based on this concept have been demonstrated [23–25]. However, an electrically injected optoelectronic "meta-atom" device (a laser or a detector) has yet to be demonstrated. In addition to the intrinsically small RC constant, the resonant LC geometry is appealing since it provides new degrees of freedom with respect to conventional photonic cavities: loss and radiation in-coupling can be engineered via critical coupling/free-space impedance matching, frequency tuning via external lumped elements, choice of the absorption directivity via antenna design, etc.

### Device Concept, Modelling, and Fabrication
In this letter, we report meta-atom QWIP detectors with dimensions below the diffraction limit ($\lambda$⁄2) operating around 3 THz with an ultra-fast response. The device concept is illustrated in

Fig. 1(a). The device core is a sub-wavelength-sized metal – semiconductor – metal (MSM) capacitor, shown in blue in Figs. 1(a) and 1(b), which hosts the detector active region, connected to a suspended metallic loop antenna providing inductance. We have shown in Ref. [24] that a similar object behaves as an LC circuit, where the capacitance and the inductance are set by the geometry. Because of this circuital character, the MSM capacitor can be extremely sub-wavelength, while still permitting electromagnetic (EM) resonance. However, electrical injection in this system has proved to be challenging. Here, we have finally solved this problem by patterning the ground plane into two separated regions, with the gap between the two defining an additional capacitance (C gap). This forces the DC detector current to flow through the active core, while C gap only marginally affects the electromagnetic resonance in the THz range. The equivalent circuit is shown in Fig. 1(b). Figure 1(c) shows optical microscope and SEM images of an array of devices, as well as an SEM image of a single detector pixel.

To highlight the key role of the small loop antenna as a receiving element for THz radiation, the optical response of the structure under illumination with a normally incident plane wave has been simulated with a commercial finite element solver (Comsol Multiphysics). The results are shown in Fig. 2. When the antenna is not present and the sub-wavelength MSM capacitor alone is considered, a Fano-like feature appears in the reflectivity spectrum around 3.5 THz (Fig. 2, dashed-dotted grey line, top panel): it arises from the Wood's anomaly of the grating created by the sub-wavelength openings in the ground plane [26, 27]. Importantly, the ohmic dissipation in the MSM cavity as a function of excitation frequency reveals that no energy is dissipated in the active region: the MSM capacitor size is much smaller than the wavelength; hence no optical mode is available for coupling. It is instead the suspended antenna that enables THz radiation coupling in the full device. When the antenna is present, the electronic LC resonance appears and yields the resonant response shown by the black solid line in Fig. 2 (top panel). Energy is now resonantly dissipated into the active region (Fig. 2, bottom panel). Note: the hybrid mode resulting from the coupling of the LC mode with the grating results in a larger resonant absorption bandwidth (3-4.5 THz), which is beneficial for detector operation.

Driven by these results, arrays and individual meta-atom detectors have been fabricated using standard micro-fabrication techniques [Fig. 1(c)] (see Supplement 1 for further details). The diameter of the active region is only 4 μm, i.e., only $\lambda/25$ for operation between 2 and 4 THz. The surface area of the array is about 350 μm × 300 μm and contains 300 single elements. The semiconductor material used in this work (wafer L1258) is a copy of the structure V267 proposed and extensively studied in Ref. [14]. It presents an operating window of about 1.5 THz between 2 and 3.5 THz, as confirmed by a preliminary characterization in a standard mesa geometry (see Supplement 1).

**Optical and Electrical Characterization**

A complete optical and electrical characterization of the fabricated samples has been performed (details of the experimental arrangement are given in Supplement 1).

Figure 3(a) shows the low temperature (4.5 K) photocurrent spectrum of an array of meta-atom detectors at different polarizations of the incident beam. As expected from the literature, as well as from the mesa characterisation, the spectrum is centred around 3THz. A clear polarization-sensitive response is observed: maximum coupling is achieved when the magnetic field of the incident beam is orthogonal to the antenna (red curve), confirming the numerical results presented in Fig. 2. A residual coupling in the other polarization (blue curve) is probably due to the nonzero $E_z$ component, given by the finite numerical aperture of the lens focusing the incident beam. Furthermore, we have measured the photocurrent spectra from several single meta-atom

detectors, individually contacted. They show a response similar to the array configuration [inset of Fig. 3(a)], thus confirming that the device arrays operate as optoelectronic meta-surfaces, where the total response is the (incoherent) sum of the individual meta-atom contributions.

Figure 3(b) shows the device dark current at 4.5 K (black curve), and under illumination from a 300 K blackbody (red curve, more details in Supplement1). The operating current densities are in agreement with this type of QWIP design. However, because of the extremely small surface of the detector active region, the operating currents have record low values in the 1–10 nA range. For instance, in these devices, the combined semiconductor surface in a 350μm × 300μm array is only3.6%. The background-limited infrared photodetection temperature (TBLIP) of the devices is 8 K, similar to the temperature found when the same material is processed in a standard mesa detector configuration. The great reduction of the operating dark current enabled by our structures is not accompanied by an appreciable improvement of TBLIP. A basic parameter to quantify the response of a photodetector is the responsivity, defined as $R = \frac{I_{photocurrent} - I_{dark}}{P_{incident}}$, where $P_{incident}$ is the power impinging on the device array, estimated at about 20nW (see Supplement 1). It can be readily evaluated by using Planck's law for a 300 K ideal blackbody upon integration of the spectral radiance over the detector sensitivity window previously measured. From the dark/light characterizations we can extract the responsivity of an array of meta-atom QWIPs, as shown in Fig. 3(c). The experimental values are in agreement with the literature, both for a detector processed as a large mesa [14] or as small patch cavities [21]. We can conclude, therefore, that the massive reduction in size of the detector preserves the performance of the QWIP material.

### RF Response

We now prove that these detectors exhibit ultra-fast speed. First, we performed a direct optical response analysis, using an RF modulated THz quantum cascade laser (QCL) as the source, and connecting the amplified output of a meta-atom detector array to a spectrum analyser (SA), as shown in Fig. 4(a). The laser used is a single-mode 3 THz surface-emitting QCL [28], biased in continuous wave (CW) just under threshold. The signal from a RF synthesizer (13 dBm) is injected using a bias-T. The effect is to switch the laser on and off at the RF frequency. Figure 4(b) shows the QWIP signal, detected after amplification, when the THz laser is modulated at 1.5 GHz. The noise floor is −82 dBm (laser shielded), for a resolution bandwidth of 1 kHz. With the laser on the detector, the SA reveals a signal at the RF modulation frequency with ∼4 dB intensity above the noise. Finally, Fig. 4(c) shows the SA signal for RF modulation frequencies of 0.5(13dBm), 1.5(13dBm), and 2.5GHz(15dBm).This demonstrates that the meta-atom detector can operate at speeds at least up to 2.5 GHz.

To gain deeper insight into the high-frequency response of this detector architecture, we have measured the complex one port S parameters (real and imaginary part of $S_{11}$) of several single-pixel and arrays of detectors, using a 40 GHz network analyser. In Fig. 5(a), the data for a representative single device (red curve, top panel) and an array (red curve, bottom panel) are plotted as normalized impedances z=$Z_L$/$Z_0$ ($Z_L$ is the device impedance loading the $Z_0$ = 50Ω measurement line) on a Smith chart. Note: the measurements were made at room temperature; the Smith chart summarizes the real and imaginary part of the $S_{11}$ parameter on a single plot.

The Smith plot confirms that, as expected, the device subwavelength size prevents a good impedance matching with the 50 Ω line over the entire frequency range.

We have inferred the equivalent RF circuit of each device by fitting the predicted behaviour (blue curves) against the experimental data (red curves) using commercial circuit simulation software (Keysight ADS). Figure 5(b) shows the equivalent circuit of a single meta-atom detector, including the access contact lines. The circuit modelling the actual detector (within the dashed brown line) comprises the parallel combination of the capacitance $C_c$ and resistance $R_c$ that models the Au-Ti/n-GaAs Schottky contact situated on top of the MSM capacitor. This junction is in series, with a resistor $R_{AR}$ accounting for the resistance of the semiconductor active core, and the resistance of the bottom ohmic Pd–Ge contact. The geometric capacitance of the MSM cavity $C_{AR}$ appears in parallel across the contacts, while the inductive behaviour of the current-carrying metallic parts (including the small loop THz antenna) is modelled with a series inductor L. Finally, $R_a$ is the access resistance, and $C_a$ is the capacitance of the large bonding pad. The averaged values extracted from five devices are reported in the inset in Fig. 5(b). $C_{AR}$ and $C_c$ are comparable with the estimate based on analytical formulas for the geometric and Schottky capacitance ($C_{AR}$ ~1 fF and $C_c$ ~50 fF). Also, the extracted series resistance $R_{AR}$ is of the same order of magnitude as the one extracted from the DC I–V curves (typically a few kΩ). This model fits the data well [blue and red curves in Fig. 5(a)] both for a single pixel and an array of devices. Note: in the latter case, the equivalent circuit is just a 2D array of single-pixel equivalent circuits, with small parasitic L and C added between neighbouring elements to account for mutual coupling.

The excellent agreement between predicted and experimental values suggests the use of the equivalent circuit as a predicting tool for the detector's high-frequency behaviour. In particular, the RF signal extraction efficiency can be simulated over a broad frequency range: if a (photo)current generator is added in series to $R_{AR}$, the ratio between the extracted current ($I_{out}$) and generated photocurrent in the active region ($I_{in}$) as a function of frequency can be calculated. The result is shown in Fig. 5(c): the solid black curve represents the frequency response of a single pixel from 100 MHz to 1 THz using the R, L, C values of Fig. 5(b) that correspond to the present experimental configuration. The modelling reveals that the Schottky capacitance $C_c$ limits the low-frequency current extraction, while the high-frequency cut off—which in these devices is tens of GHz—is limited only by the pad capacitance $C_a$. As expected, extremely subwavelength detectors lead to high-frequency operation, possibly reaching the upper bandwidth limit imposed by the QWIP transport mechanisms (BW ~30 GHz if we assume $\tau_{photocarrier} \approx 5$ ps [29, 30].

**Conclusions**

In conclusion, we have demonstrated THz detectors based on a 3D meta-atom geometry with ultrafast response. We have exploited an LC approach to drastically reduce the effective detector area, going beyond the intrinsic limitation given by the RC constant of diffraction-limited THz structures such as mesas or patch antennas.

Future developments will focus on achieving better response at low response frequencies, replacing the top Schottky contact with an alloyed ohmic contact [Fig. 5(c), solid grey curve]. Additionally, a further reduction of the contact pad capacitance [e.g., by a factor 10 in Fig. 5(c), dashed grey curve] can push the RC high-frequency cut-off to higher frequency. This is of interest in view of using these detectors in combination with mode-locked THz(QC) lasers [8, 9, 31], which is another important vista of this work. Finally, the extraction efficiency of the RF signal is only a few percent due to the impedance mismatch arising from the very small detector size and the read-outline. This is a known problem in RF technology. It can be overcome, over a small bandwidth around a chosen precise modulation frequency [32], by impedance matching to 50 Ω using discrete reactive components (inductors, capacitors).

**Acknowledgment**
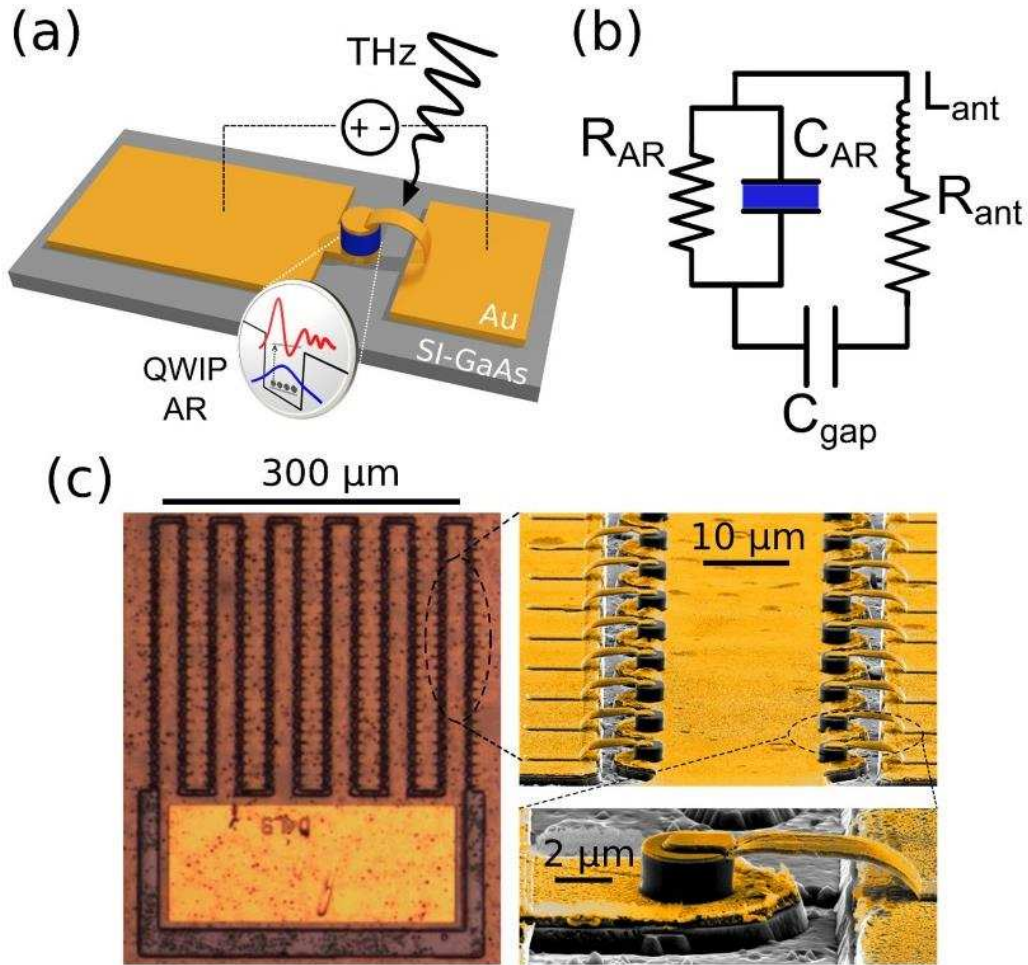
**Figure 1:**
(a)      Schematic diagram of the sub-wavelength meta-atom detector (single pixel): a MSM micro-capacitor hosting the QWIP active region is loaded with a small loop antenna. A narrow opening in the ground plane below the antenna allows the device to be biased and a photocurrent extracted.
(b)      RLC equivalent circuit: the meta-atom LC resonance is set by the MSM capacitance ($C_{AR}$) and the antenna inductance ($L_{ant}$). $R_{AR}$ and $R_{ant}$ are the active region and antenna resistances, respectively. $C_{gap}$ is the capacitance arising from the opening in the gold ground plane.
(c)      Pictures of the fabricated sample, at increasing magnification: optical microscopy image of the meta-atoms arranged in array geometry (left panel); SEM picture of the same array (right top panel); and, close view of a single meta-atom (right bottom panel). The SEM images have been coloured to highlight the metallic regions.
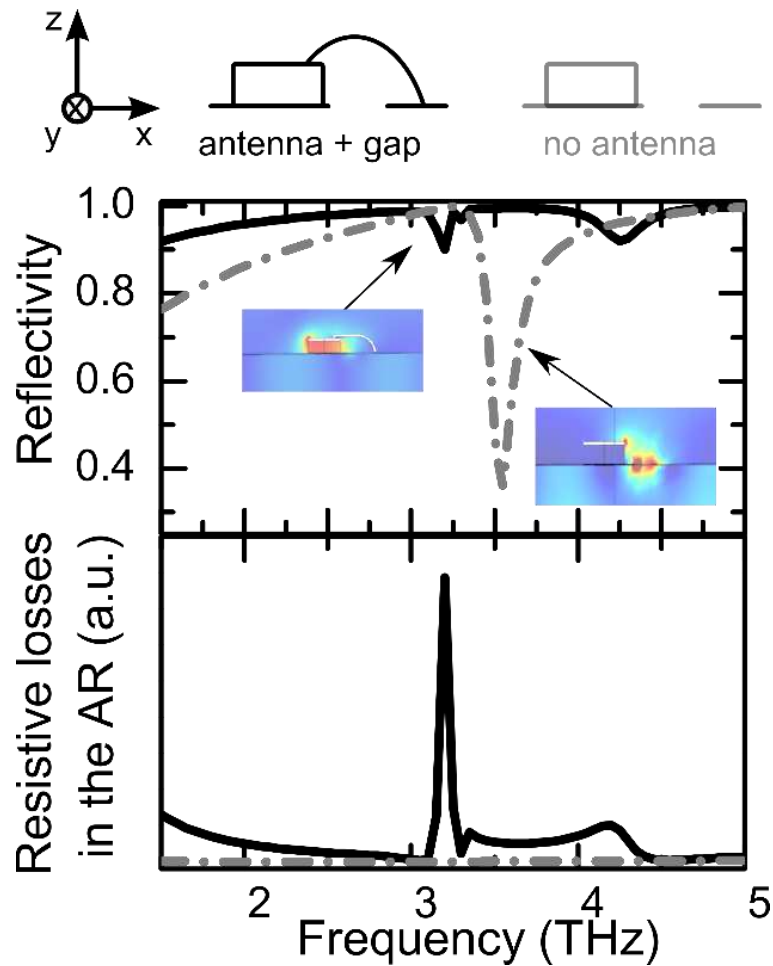
**Figure 2:**
Simulated optical response of an array of meta-atoms illuminated by normally incident THz radiation. Top panel: reflectivity spectra. When the antenna is not present and the MSM capacitor alone is considered (grey dashed–dotted line), the spectrum shows a grating mode due to the sub-wavelength openings in the ground plane; when the antenna is added (black solid line), the meta-atom LC resonance appears. Bottom panel: ohmic dissipation computed in the MSM cavity as a function of the excitation frequency, revealing that energy is resonantly dissipated in the semiconductor only if the inductive antenna completes the RLC circuit (see Supplement 1 for further details).
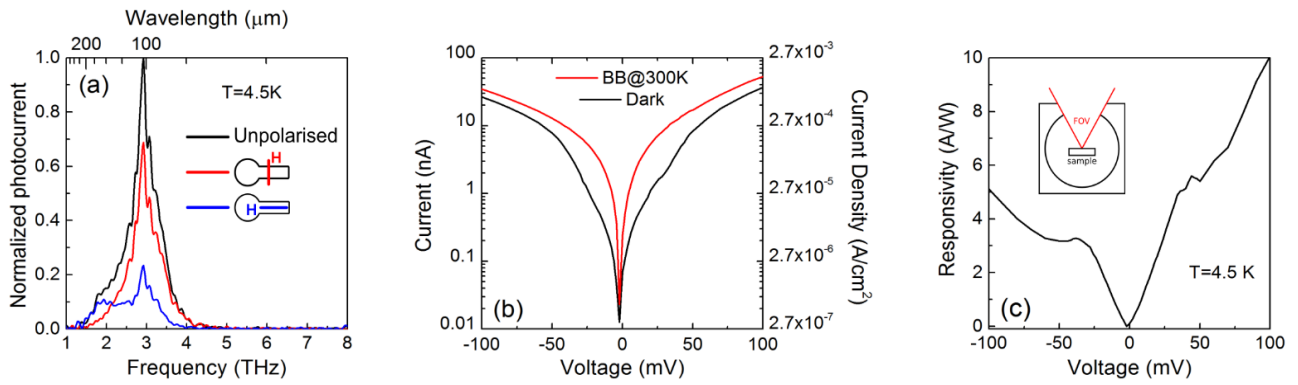
**Figure 3:**

(a)     Photo-current spectra from an array of 300 meta-atom detectors for unpolarised (black curve) and polarized (red and blue curves) radiation from a Hg lamp: THz radiation is fed into the device when the magnetic field is orthogonal to the antennas.

(b)     Typical current-voltage curves under dark conditions (black solid line) and under illumination from a 300 K black body (red solid line) for an array of meta-atom detectors.

(c)     Estimated array responsivity. The inset clarifies the definition of the field of view (FOV) of the detector inside the cryostat. All the measurements are performed     at 4.5 K.
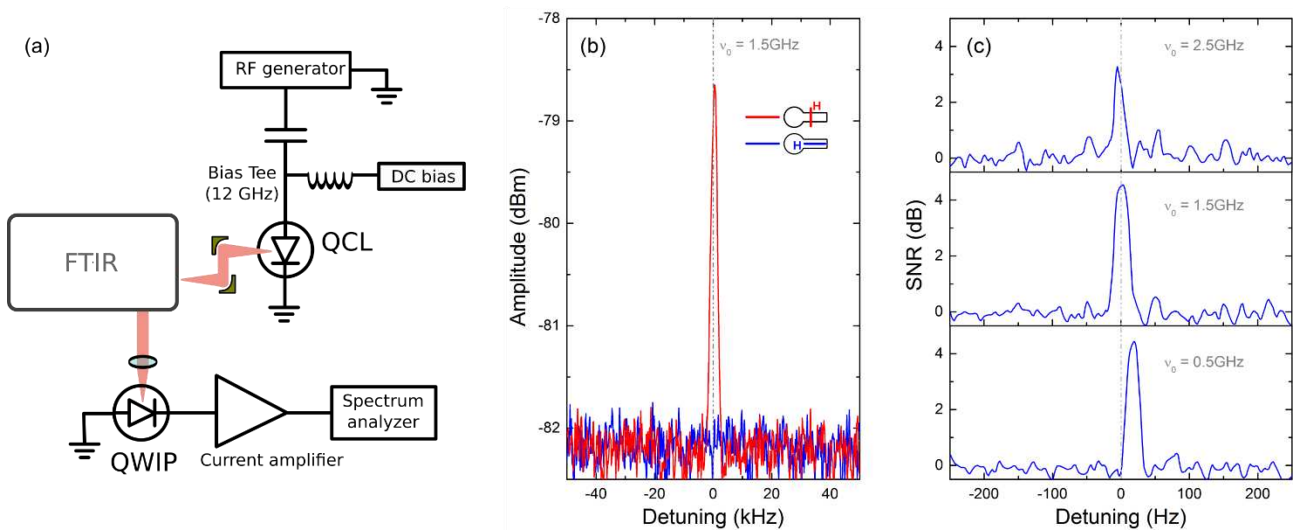
**Figure 4:**

All-optical detection of ultrafast THz signals.

(a)    Sketch of the experimental arrangement: the emitter is an RF-modulated THz QCL operating in continuous wave (f=3 THz, I=220 mA, T=10 K). The receiver is an unbiased meta-atom array (T=5 K), and the RF signal is recovered on a spectrum analyser after an amplification stage.

(b)    RF spectrum measured when the QCL is modulated at 1.5 GHz ($P_{RF}$=13 dBm, 30 dB amplification). Two polarizations are shown: magnetic field orthogonal (red curve) and parallel (blue curve) to the antennas. The latter is taken as a noise-reference.

(c)    Normalized RF spectra acquired when the QCL is driven at 0.5, 1.5 and 2.5 GHz ($P_{RF}$=13dBm, 20 dB amplification).

| $R_c$ | $C_c$ | $R_{AR}$ | $C_{AR}$ | L | $C_a$ | $R_a$ |
|-------|-------|----------|----------|------|-------|-------|
| 30 kΩ | 20 fF | 1 kΩ | 1 fF | 20 pH | 60 fF | 10 Ω |
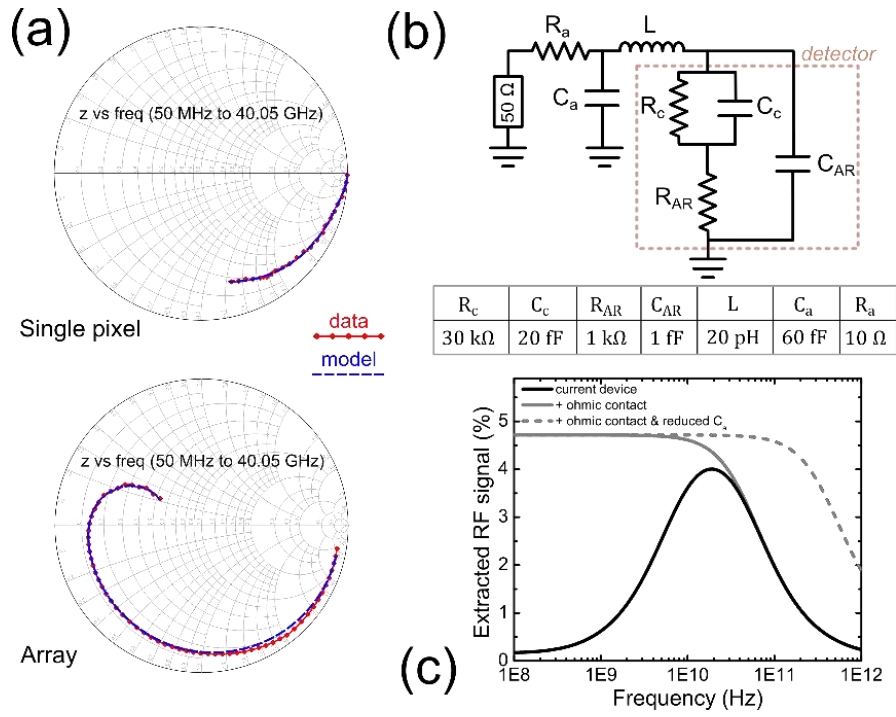
**Figure 5:**

(a)    Normalized detector impedance $z = Z/Z_0$ as a function of frequency for a single meta-atom and an array: experimental (red symbols) *vs* equivalent circuit model (blue dashed line). The measurement range is 0.05 - 40 GHz. The Smith chart summarizes the *real* and *imaginary* part of the $S_{11}$ parameter on a single plot.

(b)    Equivalent circuit of a single meta-atom detector, including the access contact lines. The circuit modelling the actual detector (within the dashed brown line) comprises the parallel combination of the capacitance $C_c$ and resistance $R_c$ that models the Au-Ti/n-GaAs Schottky contact situated on top of the MSM capacitor. This junction is in series with a resistor $R_{AR}$ accounting for the resistance of the semiconductor active core, and the resistance of the bottom ohmic Pd-Ge contact. The geometric capacitance of the MSM cavity $C_{AR}$ appears in parallel across the contacts while the inductive behaviour of the current-carrying metallic parts (including the small loop THz antenna) is modelled with a series inductor L. Finally, $R_a$ is the access resistance and $C_a$ is the capacitance of the large bonding pad.

(c)    Extracted RF signal $I_{extr}/I_{photo}$ (simulation) as a function of frequency for: (i) a single detector in the actual geometry (full black line), (ii) a single detector with top ohmic contact (full grey line), (iii) a single detector with top ohmic contact and reduced contact pad capacitance (dashed grey line). It appears that the *low-frequency* behaviour is limited by the Schottky/Ohmic contact, while the *high-frequency* behaviour - as expected - is solely limited by the system RC constant.

11

# References

1.  Sizov, F. & Rogalski, A. THz detectors. *Prog. Quantum Electron.* **34,** 278–347 (2010)

2.  Milostnaya, I. *et al.* Superconducting Single Photon Nanowire Detectors Development for IR and THz Applications. *J. Low Temp. Phys.* **151,** 591–596 (2008).

3.  Lisauskas, A., Boppel, S., Mundt, M., Krozer, V. & Roskos, H. G. Subharmonic Mixing With Field-Effect Transistors: Theory and Experiment at 639 GHz High Above fT. *IEEE Sens. J.* **13,** 124–132 (2013).

4.  Dietze, D. *et al.* Efficient population transfer in modulation doped single quantum wells by intense few-cycle terahertz pulses. *New J. Phys.* **15,** 65014 (2013).

5.  Green, B. *et al.* High-Field High-Repetition-Rate Sources for the Coherent THz Control of Matter. *Sci. Rep.* **6,** 22256 (2016).

6.  Rösch, M., Scalari, G., Beck, M. & Faist, J. Octave-spanning semiconductor laser. *Nat. Photonics* **9,** 42–47 (2014).

7.  Burghoff, D. *et al.* Terahertz laser frequency combs. *Nat. Photonics* **8,** 462–467 (2014).

8.  Barbieri, S. *et al.* Coherent sampling of active mode-locked terahertz quantum cascade lasers and frequency synthesis. *Nat. Photonics* **5,** 306–313 (2011).

9.  Wang, F. *et al.* Generating ultrafast pulses of light from quantum cascade lasers. 1–17

10. Wang, F. *et al.*, "Short terahertz pulse generation from a dispersion compensated modelocked semiconductor laser," Laser Photon. Rev. **11,** 1700013 (2017).

11. Koppens, F. H. L. *et al.* Photodetectors based on graphene, other two-dimensional materials and hybrid systems. *Nat. Nanotechnol.* **9,** 780–793 (2014).

12. Mittendorff, M. *et al.* Ultrafast graphene-based broadband THz detector. *Appl. Phys. Lett.* **103,** 21113 (2013)

13. Schneider, H. (Harald) & Liu, H. C. *Quantum well infrared photodetectors: physics and applications*. (Springer, 2007).

14. Luo, H., Liu, H. C., Song, C. Y. & Wasilewski, Z. R. Background-limited terahertz quantum-well photodetector. *Appl. Phys. Lett.* **86,** 231103 (2005).

15. Durmaz, H., Nothern, D., Brummer, G., Moustakas, T. D. & Paiella, R. Terahertz intersubband photodetectors based on semi-polar GaN/AlGaN heterostructures. *Appl. Phys. Lett.* **108,** 201102 (2016).

16. Li, H. et al., "6.2-GHz modulated terahertz light detection using fast terahertz quantum well photodetectors," Sci. Rep. **7,** 3452 (2017)

17. Grant, P. D. *et al.* Terahertz free space communications demonstration with quantum cascade laser and quantum well photodetector. *Electron. Lett.* **45,** 952 (2009).

18. Wang, C., Cao, J., Gu, L., Wu, Q. & Tan, Z. 20 Mbps wireless communication demonstration using terahertz quantum devices. *Chinese Opt. Lett. Vol. 13, Issue 8, pp. 081402-* **13,** 81402 (2015).

19. Vardi, A. *et al.* High-speed operation of GaN/AlGaN quantum cascade detectors at λ≈1.55 μm. *Appl. Phys. Lett.* **93,** 193509 (2008).

20. Zhang, R. *et al.*, "Metal-grating-coupled terahertz quantum-well photodetectors," IEEE Electron Device Lett. **32,** 659–661 (2011).

21. Palaferri, D. *et al.* Patch antenna terahertz photodetectors Patch antenna terahertz photodetectors. **161102,** 1–6 (2015).

22. Benz, A. *et al.*, "Resonant metamaterial detectors based on THz quantum-cascade structures," Sci. Rep. **4,** 4269 (2014).

23. Fan, K., Strikwerda, A. C., Zhang, X. & Averitt, R. D. Three-dimensional broadband tunable terahertz metamaterials. *Phys. Rev. B* **87,** 161104 (2013).

24. Paulillo, B. *et al.* Circuit-tunable sub-wavelength THz resonators: hybridizing optical cavities and loop antennas. *Opt. Express* **22,** 21302–21312 (2014).

25. Paulillo, B. *et al.* Room temperature strong light-matter coupling in three dimensional terahertz meta-atoms. *Appl. Phys. Lett.* **108,** 101101 (2016).

26. Genet, C. & Ebbesen, T. W. Light in tiny holes. *Nature* **445,** 39–46 (2007).

27. Miroshnichenko, A. E., Flach, S. & Kivshar, Y. S. Fano resonances in nanoscale structures. *Rev. Mod. Phys.* **82,** 2257–2298 (2010).

28. Xu, G. *et al.* Surface-emitting terahertz quantum cascade lasers with continuous-wave power in the tens of milliwatt range. *Appl. Phys. Lett.* **104,** 1–5 (2014).

25. B. Paulillo, J.-M. Manceau, L. H. Li, A. G. Davies, E. H. Linfield, and R. Colombelli, "Room temperature strong light-matter coupling in three dimensional terahertz meta-atoms," Appl. Phys. Lett. 108, 101101 (2016).

26. C. Genet and T. W. Ebbesen, "Light in tiny holes," Nature 445, 39 –46 (2007).

27. A. E. Miroshnichenko, S. Flach, and Y. S. Kivshar, "Fano resonances in nanoscale structures," Rev. Mod. Phys. 82, 2257–2298 (2010).

28. G. Xu, L. Li, N. Isac, Y. Halioua, A. Giles Davies, E. H. Linfield, and R. Colombelli, "Surface-emitting terahertz

quantum cascade lasers with continuous-wave power in the tens of milliwatt range," Appl. Phys. Lett. 104, 091112 (2014).

29. H. C. Liu, C. Y. Song, A. J. SpringThorpe, and J. C. Cao, "Terahertz quantum-well photodetector," Appl. Phys. Lett. 84, 4068–4070 (2004).

30. H. C. Liu, G. E. Jenkins, E. R. Brown, K. A. McIntosh, K. B. Nichols, and M. J. Manfra, "Optical heterodyne detection and microwave rectification up to 26 GHz using quantum well infrared photodetectors," IEEE Electron Device Lett. 16, 253–255 (1995).

31. D.Bachmann, M.Rösch, M.J.Süess, M.Beck, K.Unterrainer, J.Darmo, J. Faist, and G. Scalari, "Short pulse generation and mode control of broadband terahertz quantum cascade lasers," Optica 3, 1087–1094 (2016).

32. Pozar, D. M. *Microwave engineering*. (Wiley, 2012).